FERROELECTRICS

Giant tunneling electroresistance in sliding ferroelectrics

Yue Wang[1,2], Yu Zhao[1], Yifei Zhang[1,2], Liutianyi Zhang[1,2], Zijian Zhong[1,2], Sishuo Liu[3], Chentao Hou[1], Fanxin Liu[4], Bin-Bin Zhang[5], Zhongming Wei[1,2], Yue-Yang Liu[1,2], Han Wang[3,6]*, Ping-Heng Tan[1,2]*, Jiangbin Wu[1,2]*

Nonvolatile memories should store information reliably while consuming little energy. Ferroelectric tunnel junctions offer compact readout, but conventional ionic displacement ferroelectrics can fatigue, and two-dimensional sliding ferroelectrics are robust but generate weak readout in two terminal devices. We engineered a van der Waals junction using rhombohedral molybdenum disulfide, hexagonal boron nitride, monolayer graphene, and chromium. This architecture converts small sliding polarization into synergistic modulation of tunneling barrier height and carrier concentration. The devices showed tunneling electroresistance above 10 million, a high conductance state current density of 222 amperes per square centimeter at 0.5 volts, and an endurance beyond 100 billion cycles while switching with 13-nanosecond pulses at an estimated energy of 6.5 femtojoules, offering a route to compact low-power memory.

Data movement between logic and memory increasingly dominates energy consumption and latency, and these issues have spurred interest in densely integrated, two-terminal nonvolatile memories with fast operation (*1*–*5*). A central challenge in such nanoscale stacks is that giant readout contrast and ultrahigh endurance rarely coexist. More endurance-favored switching pathways generally perturb the active material less, but they also tend to produce a much smaller two-state current readout window (*1*, *6*–*11*). For example, ferroelectric tunnel junctions (FTJs), in which polarization reversal modulates an ultrathin tunneling barrier, can deliver very large tunneling electroresistance (TER $>10^7$) (*12*–*14*). However, in conventional ionic-displacement ferroelectrics, repeated switching is often accompanied by defect accumulation and interfacial degradation associated with ionic motion, vacancy migration, and domain-wall pinning, which eventually compromises reliability and endurance ($<10^7$ switching cycles) (*7*, *15*). Achieving both a large electrical contrast and nearly fatigue-free cycling remains a fundamental materials-and-device challenge for compact two-terminal memories.

Two-dimensional (2D) sliding ferroelectrics such as 3R-MoS_2 (*8*, *16*) and 1T′-ReS_2 (*17*, *18*) can strongly suppress polarization fatigue and sustain cycling up to $\sim10^{11}$ operations because their polarization arises from elastic interlayer translation rather than ionic displacement (*19*–*21*). However, this advantage has not naturally translated into two-terminal FTJs with high TER. Their remanent polarization is only 0.1 to 0.3 $\mu C\ cm^{-2}$, two to three orders of magnitude less than that of conventional oxide ferroelectrics of 10 to 100 $\mu C\ cm^{-2}$ (Fig. 1A) (*16*, *18*, *22*, *23*). The small polarization-induced potential shift is easily screened by metallic electrodes and yields only weak barrier modulation, low TER, and limited ON-state current in standard two-terminal stacks (*17*, *18*).

[1]State Key Laboratory of Semiconductor Physics and Chip Technologies, Institute of Semiconductors, Chinese Academy of Sciences, Beijing, China. [2]Center of Materials Science and Optoelectronics Engineering, University of Chinese Academy of Sciences, Beijing, China. [3]Department of Electrical and Electronic Engineering, University of Hong Kong, Hong Kong SAR, China. [4]School of Physics, Zhejiang University of Technology, Hangzhou, China. [5]College of Advanced Interdisciplinary Studies and Nanhu Laser Laboratory, National University of Defense Technology, Changsha, China. [6]Zhangjiang Laboratory, Pudong, Shanghai, China. *Corresponding author. Email: hanwang@eee.hku.hk (H.W.); phtan@semi.ac.cn (P.-H.T.); jbwu@semi.ac.cn (J.W.)

Thus, many sliding-ferroelectric devices have relied on three- or four-terminal schemes that decouple programming from readout, which increases structural complexity and decreases integration density (*8*, *19*). A two-terminal architecture that can convert weak sliding polarization into a strong tunneling response would circumvent these issues.

Here, we show that such conversion can be achieved in a two-terminal FTJ through a van der Waals (vdW) stack comprising chromium (Cr)/hexagonal boron nitride (h-BN)/3R-MoS_2/graphene. In this sliding FTJ, h-BN ensures a uniform, leakage-suppressing tunneling barrier, and graphene provides a weakly screening, low-density-of-states electrode. Their combined electrode-barrier engineering converts small, polarization-induced band bending into an effective synergistic modulation of the tunneling barrier and carrier injection and extraction. As a result, these two-terminal junctions deliver TER $>10^7$ with an ON-state current density (J_{ON}) of up to 222 A cm^{-2} at the read bias of 0.5 V. These devices enable fast, low-voltage readout and preserve fatigue-resistant endurance exceeding 10^{11} cycles, as well as stable retention. We further reproduced the bistable nonvolatile switching in FTJs based on 1T′-ReS_2, supporting the broader applicability of this design principle. This vdW architecture breaks the usual coupling between readout margin and cycling degradation in a compact, two-terminal stack and opens a route toward dense, nonvolatile memories and crossbar in-memory computing.

Sliding ferroelectricity in 3R-MoS_2

2D sliding ferroelectrics arise from interlayer vdW sliding rather than from ionic displacement (*21*). In these materials, for example, 3R-MoS_2, relative in-plane translation between adjacent layers changes the stacking from a high-symmetry to a low-symmetry configuration, which breaks inversion or mirror symmetry and thereby generates spontaneous polarization through asymmetric charge redistribution (*24*). The interfacial charge density differences calculated by density functional theory (DFT) for the two energetically degenerate stacking states of bilayer 3R-MoS_2, namely AB (Fig. 1B) and BA (Fig. 1C), reveal asymmetric electron accumulation and depletion between the two MoS_2 layers that lead to out-of-plane polarization.

To verify the stacking order of the multilayer 3R-MoS_2 experimentally, we performed ultra-low-frequency Raman spectroscopy (*25*) (Fig. 1D) and optical second-harmonic generation (SHG) measurements (Fig. 1E) on one- to five-layer MoS_2 samples. The spectra showed that the lowest branch of shear ($S_{N,\ N-1}$, N is the layer number) modes was markedly stronger and redshifted monotonically (see fig. S1 for more details) as the layer number increased, which is characteristic of 3R stacking and arises from stacking-controlled Raman intensity selection rules (*26*). The thickness-dependent SHG intensity provided an independent fingerprint of the polytype (Fig. 1E and fig. S1). Across one to five layers, we observed robust SHG from both odd and even layers, and the SHG intensity increased with layer number. This response is to be expected for 3R stacking, which remains noncentrosymmetric for all layer numbers, unlike 2H stacking, in which even layers become centrosymmetric and the SHG exhibits a pronounced odd-even modulation (*27*).

To further characterize the ferroelectric response of 3R-MoS_2, we performed piezoresponse force microscopy (PFM) on 3R-MoS_2/Au structures. The local PFM spectroscopy exhibited well-defined hysteresis in both the piezoresponse amplitude and phase upon sweeping the tip bias (Fig. 1F). The amplitude loop showed the characteristic "butterfly-like" pattern expected for polarization switching, whereas the phase displayed an abrupt reversal (near 180°), indicating a reversible switching of the polarization state. The slight amplitude asymmetry between the two states arises from polarization-dependent tip-sample electrostatic interactions, in which polarization reversal alters surface-bound charge and local surface potential, thus influencing the electrostatic contribution to the PFM response (*28*). Together, these concurrent amplitude-phase hysteresis features provided direct nanoscale evidence for switchable ferroelectricity in 3R-MoS_2.

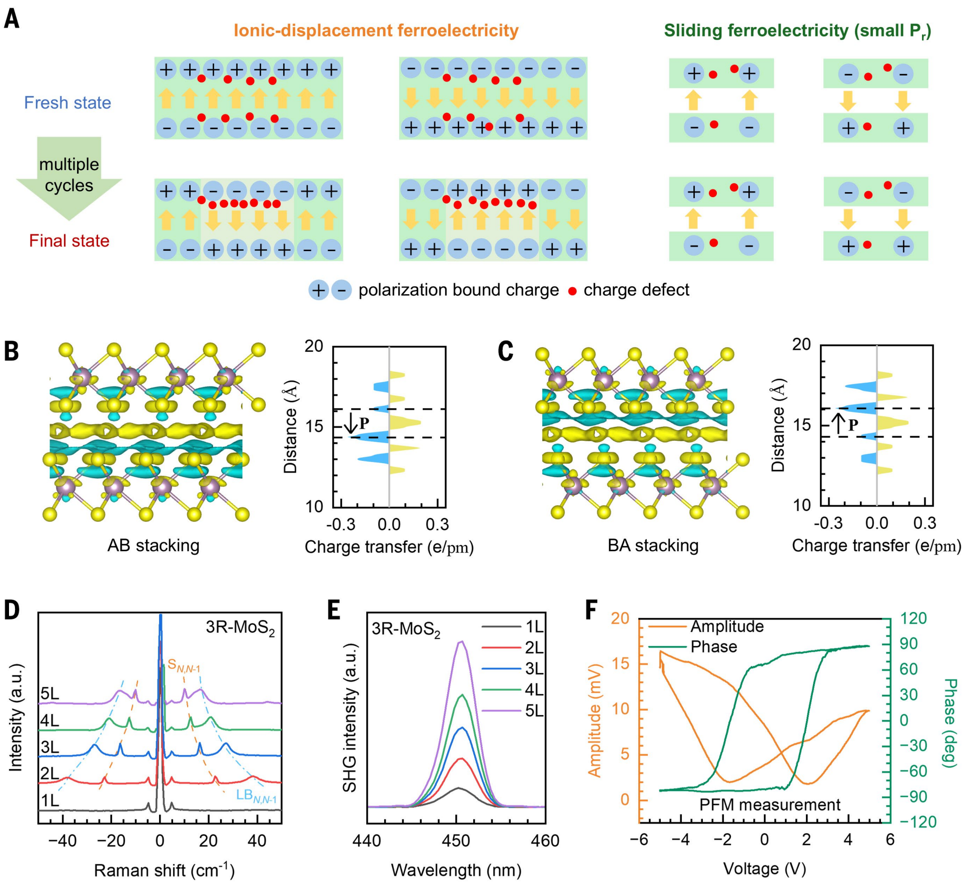

Fig. 1. Sliding ferroelectricity in 3R-MoS₂. (**A**) Comparison of switching mechanisms. Conventional ionic-displacement ferroelectrics experience defect migration under repeated switching, whereas sliding ferroelectrics retain their structural integrity during cycling. (**B** and **C**) Interfacial charge distribution for AB stacking (B) and BA stacking (C). The DFT-calculated charge density difference map shows yellow regions indicating charge accumulation and blue regions of charge depletion at the interface. The line profile reveals asymmetric electron redistribution across the interface. (**D**) Layer-dependent ultra-low-frequency Raman spectra of MoS_2. Spectra collected from one to five layers show the S mode and the layer-breathing (LB) mode. The peak positions and intensities vary with layer number, consistent with a 3R stacking configuration. (**E**) Layer-dependent SHG responses of MoS_2. The presence of SHG in even layers indicates noncentrosymmetric 3R stacking. (**F**) PFM characterization of 3R-MoS_2/Au. The amplitude-voltage curve displays a butterfly-shaped loop, and the phase-voltage curve shows an ~180° reversal between opposite polarities.

Switching characteristics of sliding FTJs

We schematically outline the device layout in Fig. 2A, starting from an 8 × 8 array illustration and then zooming into a representative unit cell to highlight the vertical vdW stack, where few-layer 3R-MoS_2 was integrated with an h-BN tunneling barrier and contacted by asymmetric electrodes [a Cr top and a monolayer-graphene (1LG) bottom]. Figure 2B shows a cross-sectional bright-field scanning transmission electron microscopy (BF-STEM) image of the as-fabricated heterostructure (see fig. S2 for the optical image), revealing the continuous layered morphology and the abrupt vertical stacking sequence. From the image contrast and measured thickness, the key constituents are identified as a 1LG bottom electrode, a five-layer 3R-MoS_2 flake (~3.2 nm), and an h-BN tunneling barrier with a thickness of ~6.6 nm (~20 layers). Element-resolved electron energy-loss spectroscopy (EELS) mappings (Si, C, S, N, and Cr) further corroborated the spatial locations of the substrate, 1LG, 3R-MoS_2, h-BN, and the Cr electrode.

We next performed room-temperature electrical measurements. A full direct current (DC) sweep within ±5 V yielded a counterclockwise hysteresis with well-defined switching events (Fig. 2C). The forward sweep (positive bias) set the device into the high-conductance state at ~3.0 V, whereas the reverse sweep reset it at ~−3.4 V. To ensure complete polarization switching under pulse operation, we applied a larger voltage window than that used in the DC sweep. For quantitative TER evaluation without perturbing the programmed state, the device was first written into the high- and low-conductance states by using programming pulses of +7 V and −5 V (pulse width 1 μs), followed by readout current-voltage (*I-V*) scans restricted to a small window of −1 V to +1 V (Fig. 2D). At a read bias of 0.5 V, the junction reached an ultrahigh TER of ~1.9×10^7. The corresponding hysteresis trajectory extracted at 0.5 V (Fig. 2E, orange arrows) followed the pulse sequence −5 V → 0 V → +7 V → 0 V → −5 V with a voltage step of 0.5 V and remained counterclockwise, consistent with deterministic switching between two nonvolatile conductance states. Compared with previously reported sliding FTJs, the achieved TER represents a five-order-of-magnitude improvement (*17*, *29*).

We further fabricated an 8 × 8 sliding FTJ array with 1LG electrodes (Fig. 2F). Figure 2G summarizes the polarization-switching characteristics of all 64 devices, which exhibited consistent bistable switching. Here, the coefficient of variation (CV) is defined as the ratio of the standard deviation (σ) to the mean, and the interquartile range (IQR) is defined as the difference between the 75th and 25th percentiles. Using these metrics, the extracted switching voltages showed tight statistical distributions: The set voltage (V_{set}) clustered around 3.09 V with a standard deviation (σ_{set}) of 0.10 V (CV_{set} = 0.03), whereas the reset voltage centered at V_{reset} = −2.92 V with a σ_{reset} of 0.14 V (CV_{reset} = 0.05; fig. S3). The ON- and OFF-state read current densities (J_{ON} and J_{OFF}) at V = 0.5 V collected from the same 64 devices are presented as probability distributions in Fig. 2H. Quantitatively, the J_{ON} had a median of 1.55×10^2 A cm^{-2} (IQR = 4.32×10^1 A cm^{-2}), whereas the OFF-state current density (J_{OFF}) showed a median of 8.30×10^{-6} A cm^{-2} (IQR = 2.04×10^{-6} A cm^{-2}; fig. S3). The slight variation in the read current among different devices mainly originates from fabrication-related nonuniformities such as minor differences in residual organic contamination and effective junction area. However, these variations do not affect the stable bistable switching characteristics or the high ON/OFF ratio of the devices. These compact distributions in both switching voltages and read currents collectively demonstrate excellent device-to-device uniformity and process reproducibility, supporting the scalability of high-performance sliding FTJ arrays.

Synergistic modulation of tunneling barrier and carrier concentration

We investigated why the relatively small remanent polarization in sliding ferroelectrics can still produce an ultrahigh TER. Figure 3, A and B, schematically illustrate the band structures of the sliding FTJ in the OFF-state and ON-state, respectively, with more detailed

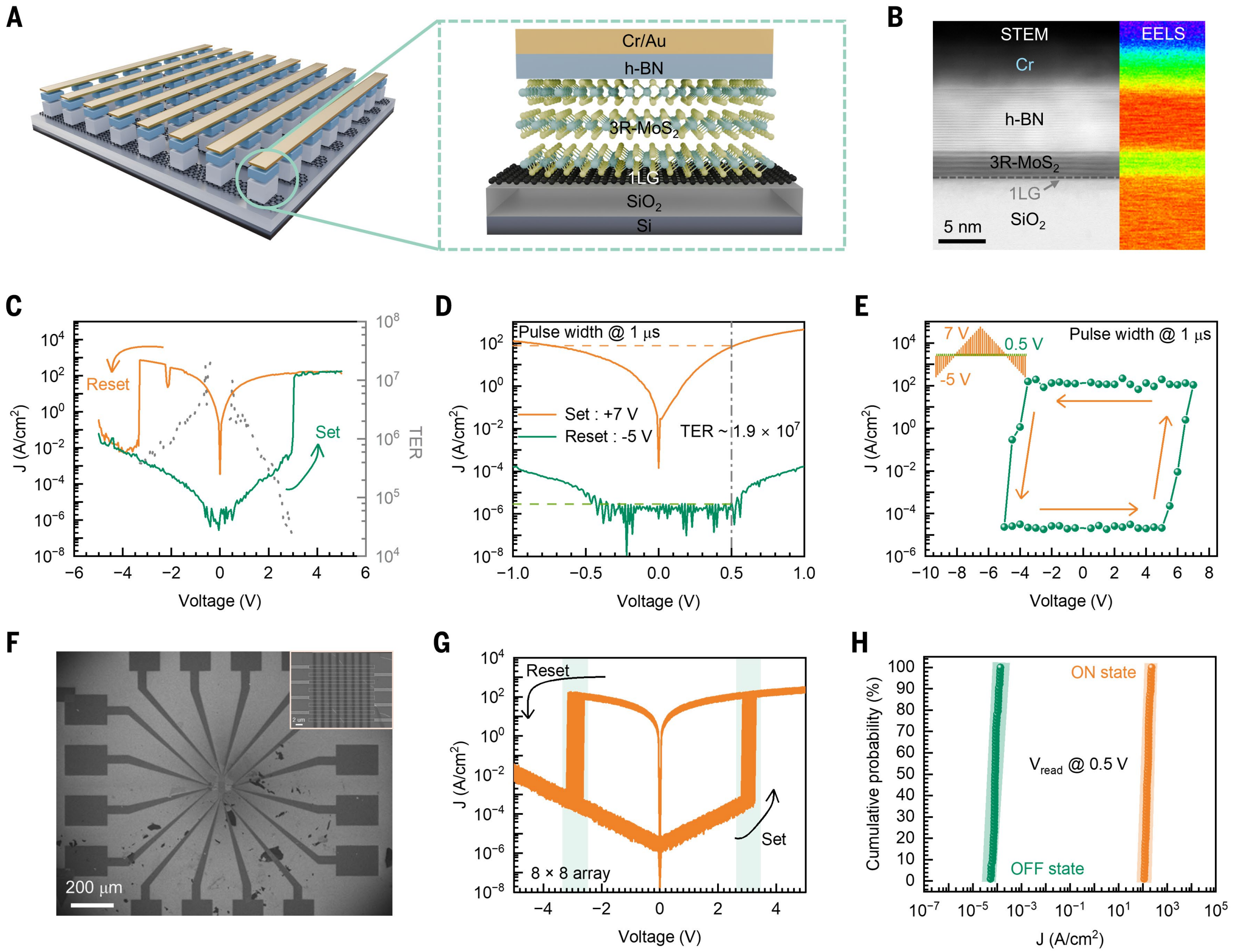

Fig. 2. Structural and electrical characteristics of the 3R-MoS_2 sliding FTJs. (**A**) Device structure and unit cell configuration. Left: overall layout of an 8×8 array. Right: representative unit cell with the vertical vdW stack. (**B**) Cross-sectional characterization of the heterostructure. BF-STEM image and EELS elemental mapping show the stacking and elemental distribution of the 1LG bottom electrode, five-layer 3R-MoS_2 flake, and h-BN tunneling barrier. (**C**) *I-V* characteristics of the device. The *I-V* relationship was measured by applying a continuous DC bias and recording the current response as a function of the applied voltage. (**D**) Readout characteristics under a small bias. *I-V* curves were measured within a read bias range of –1 V to +1 V after pulse programming. (**E**) Current response under a pulsed voltage sequence. The current as a function of pulse voltage was measured by applying a voltage pulse train (shown in the inset). (**F**) SEM image of the 8×8 array. (**G**) *I-V* curves of the 8×8 array. (**H**) ON- and OFF-state read current distributions of 64 devices.

quantitative band diagrams provided in fig. S4. We defined the polarization direction in 3R-MoS_2 such that polarization pointed from the negatively charged interface to the positively charged interface. When the polarization of 3R-MoS_2 pointed toward the 1LG electrode, the Fermi level at the h-BN and 3R-MoS_2 interface shifted downward, whereas the Fermi level near the metal electrode remained unchanged. The average tunneling barrier height increased and reduced the tunneling probability, resulting in the OFF-state. Electrons that accumulated in 3R-MoS_2 near the 1LG side could then transfer to the nearby 1LG because of the Fermi-level pinning-free vdW contact (*30*) between 3R-MoS_2 and 1LG. This carrier extraction effect reduced the effective electron concentration in 3R-MoS_2 available for tunneling and further reduced the tunneling current, leading to a lower OFF-state. By contrast, as the polarization of 3R-MoS_2 pointed toward the h-BN, the Fermi level at the interface of h-BN and 3R-MoS_2 shifted upward, leading to a lower tunneling barrier, that is, the ON-state. The polarization also increased the carrier concentration for tunneling near the h-BN, which further enhanced the tunneling current (up to 222 A cm^{-2} at a read bias of 0.5 V). The combined modulation of tunneling barrier height and carrier concentration substantially suppressed the OFF-state current and enhanced the ON-state current, resulting in an ultrahigh TER of up to 1.9×10^7.

The h-BN in this sliding FTJ provided a barrier that protected the ferroelectric polarization. In the absence of the h-BN layer, as shown in fig. S5, for the same 1LG/3R-MoS_2 stacking, when metal electrodes were directly deposited, the polarization switching window almost disappeared because of the depolarization associated with large leakage current (*31*) and screening by metal electrodes due to Fermi-level pinning at the semiconductor interface (*32*, *33*). The thin h-BN layer enabled direct tunneling, as supported by the temperature-dependent *I-V* curves in Fig. 3C and the corresponding $\ln[I(V)/V^2]$ versus $1/V$ plot in fig. S6. Once the h-BN tunneling layer became thicker (e.g., ~10.2 nm), as shown in fig. S7, the carrier transport mechanism was dominated by Fowler-Nordheim tunneling under high-electric-field conditions.

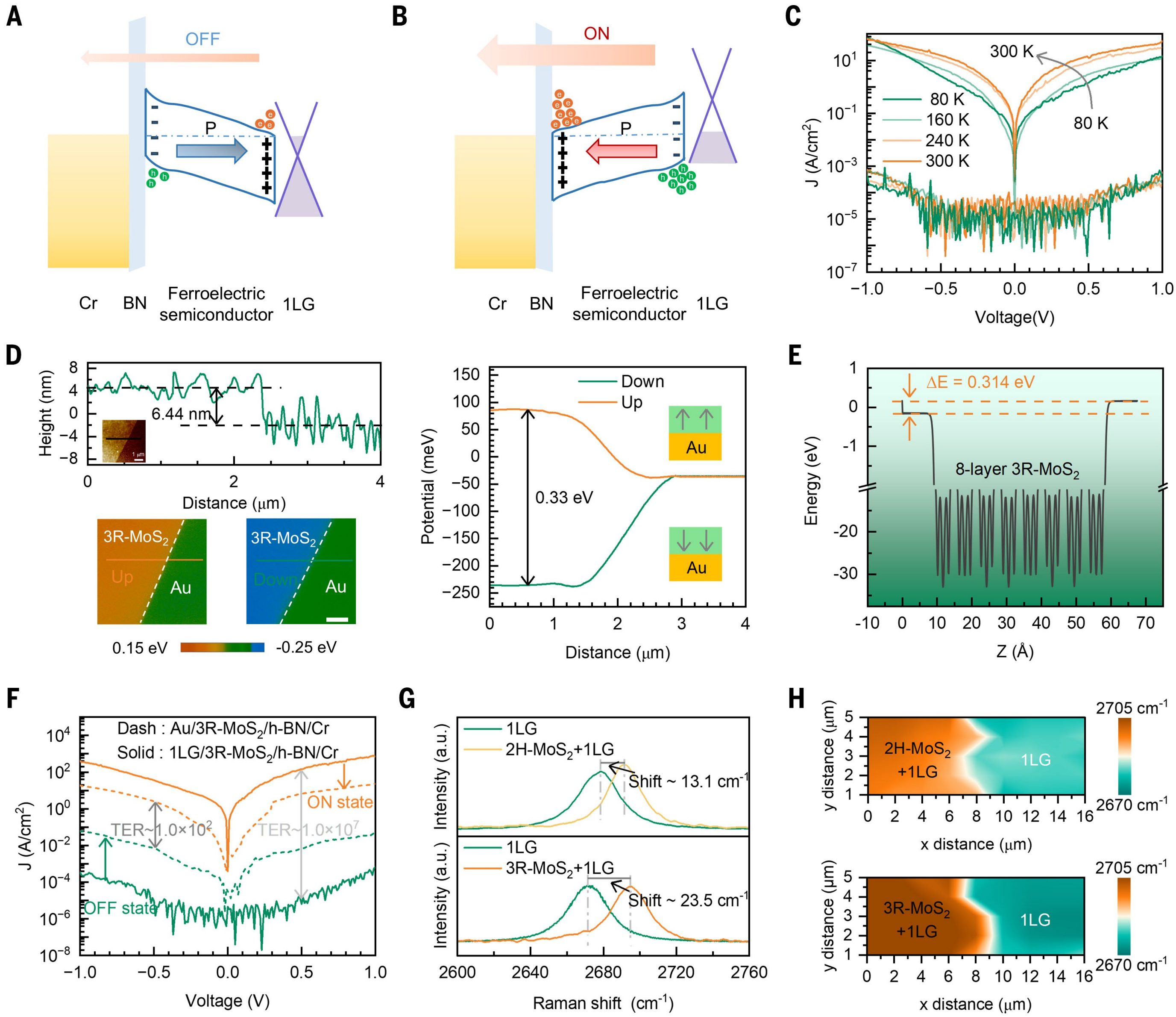

Fig. 3. Multifactor control enabling stable high TER. (**A** and **B**) Band diagrams of the sliding FTJ in the OFF-state and ON-state. (**C**) Temperature-dependent *I-V* characteristics of the device. *I-V* curves of the ON-state and OFF-state measured at 80, 160, 240, and 300 K. (**D**) Surface potential mapping of polarized 3R-MoS_2. Left, bottom: surface potential maps of 3R-MoS_2 stacked on Au after ferroelectric polarization, with polarization oriented up and down. Left, top: corresponding PFM images of 3R-MoS_2 showing the thickness used. Right: the KPFM line profile of the surface potential is extracted along the solid line in the lower panel on the left. (**E**) Electrostatic potential calculation for eight-layer 3R-MoS_2 (matching the experimental layer number). (**F**) *I-V* curves of the ON-state and OFF-state for sliding FTJs using 1LG and Au electrodes. (**G**) Raman spectra in the 2D-mode spectral range under 532-nm excitation for bare 1LG versus 1LG on 2H-MoS_2 and 1LG on 3R-MoS_2. (**H**) Spatial mapping of the graphene 2D Raman mode for bare 1LG, 1LG on 2H-MoS_2, and 1LG on 3R-MoS_2.

Thus, most of the applied voltage dropped across the thick h-BN layer and left insufficient voltage to effectively drive ferroelectric polarization switching in 3R-MoS_2, which also led to the absence of a TER window. The appropriate h-BN thickness played a key role in maintaining stable ferroelectric switching, which was essential for modulating the barrier height and obtaining a measurable TER. We further confirmed the barrier height difference between the two polarization states by Kelvin probe force microscopy (KPFM) measurements. The eight-layer 3R-MoS_2 with a thickness of ~6 nm placed on an Au substrate showed a surface potential difference of 0.33 eV between the two polarization states (Fig. 3D), consistent with previous reports (*34*, *35*). We calculated the electrostatic potential for eight-layer 3R-MoS_2 (Fig. 3E) and found a potential difference between the two surfaces of 0.314 eV, in excellent agreement with the KPFM results. The bias-dependent decay of TER with increasing read voltage provided further evidence for a barrier-height difference (Fig. 2C and fig. S8), because the OFF-state current increased disproportionately faster than the ON-state current due to its greater sensitivity to changes in barrier height (see the supplementary materials for details).

Graphene enabled carrier-concentration modulation in the sliding FTJ. Figure 3F shows that replacing the 1LG bottom electrode with Au (with the same Cr top electrode) yielded lower J_{ON} and higher J_{OFF}. Unlike 1LG, Au behaved as a rigid, strongly screening electrode with a nearly fixed Fermi level; accordingly, the Au electrode device exhibited much weaker polarization-induced carrier-concentration modulation. Raman spectra in Fig. 3G show that the graphene 2D peak blue shifted in both heterostructures of $2H\text{-}MoS_2$/1LG (~13.1 cm^{-1}) and $3R\text{-}MoS_2$/1LG after setting the polarization toward 1LG (~23.5 cm^{-1}) compared with bare 1LG. The presence of a blue shift in both stacks indicated a common origin, namely interfacial charge transfer driven by Fermi-level mismatch at the MoS_2/graphene vdW interface, which increased the carrier density in 1LG (*30*). The larger blue shift in $3R\text{-}MoS_2$/1LG further implied an additional contribution from the out-of-plane ferroelectric polarization field in $3R\text{-}MoS_2$, providing extra electrostatic doping and carrier modulation in graphene. Raman mapping (Fig. 3H) showed spatially uniform 2D peak shifts for both stackings, supporting a doping-dominant mechanism rather than local strain (*36*). Band alignment calculations (fig. S9) corroborated this model. Projected density-of-states analysis of two $3R\text{-}MoS_2$/1LG interface models with opposite out-of-plane polarization showed that the interfacial electron barrier changed from 0.06 eV (polarization pointing away from 1LG) to 0.14 eV (polarization pointing toward 1LG), providing direct evidence of polarization-controlled band alignment at the $3R\text{-}MoS_2$/graphene interface associated with charge transfer. Together, Raman, transport, and DFT consistently established that graphene functions as a polarization-tunable electrode, promoting efficient carrier injection and extraction and enhancing the electrically readable contrast.

Comprehensive device performance

To demonstrate the generalizability of vdW sliding FTJs, we also fabricated and characterized Cr/h-BN/$1T'\text{-}ReS_2$/graphene sliding FTJs. Figure S10 shows the device structure and its electrical characteristics, confirming the integrity of the vertical heterostructure and its bistable switching behavior. These results indicated that the observed nonvolatile switching was not limited to $3R\text{-}MoS_2$, but could also be achieved in other layered sliding ferroelectric semiconductors, supporting the generalizability of the mechanism. Figure 4A shows the current responses of the $3R\text{-}MoS_2$ and $1T'\text{-}ReS_2$ sliding FTJs measured using program/erase pulse pairs of identical width. Starting from the high-resistance state set by a −5 V pulse, the devices were switched to the low-resistance state by +7 V pulses as the pulse width was systematically varied.

Reliable polarization switching was maintained even when the pulse width (t_w) was reduced to 13 ns, which approached the temporal resolution limit of the measurement system, with the TER remaining nearly unchanged. Thus, the minimum switching energy (E) of this device was estimated to be ~6.5 fJ using $E = IVt_w$. The retention and fatigue endurance of the devices at room temperature are shown in Fig. 4, B and C. Retention measurements further showed that the high TER in both devices remained stable for 10^3 to 10^4 s and could be projected to 10 years, confirming the feasibility of long-term nonvolatile memory applications. Using +7 V/−5 V pulses of 100-ns width for polarization switching, both the $1T'\text{-}ReS_2$–based and the $3R\text{-}MoS_2$–based sliding FTJs maintained a stable polarization window for up to 10^{11} cycles, comparable to the state of the art. Figure 4, D and E, compare the J_{ON} performance of the devices in this work with conventional ionic-displacement ferroelectric FTJs. At a read voltage of 0.5 V, the devices achieved a J_{ON} of 222 A cm^{-2}, which was higher than that of conventional ionic-displacement devices (most of which are <50 A cm^{-2}) (table S1)

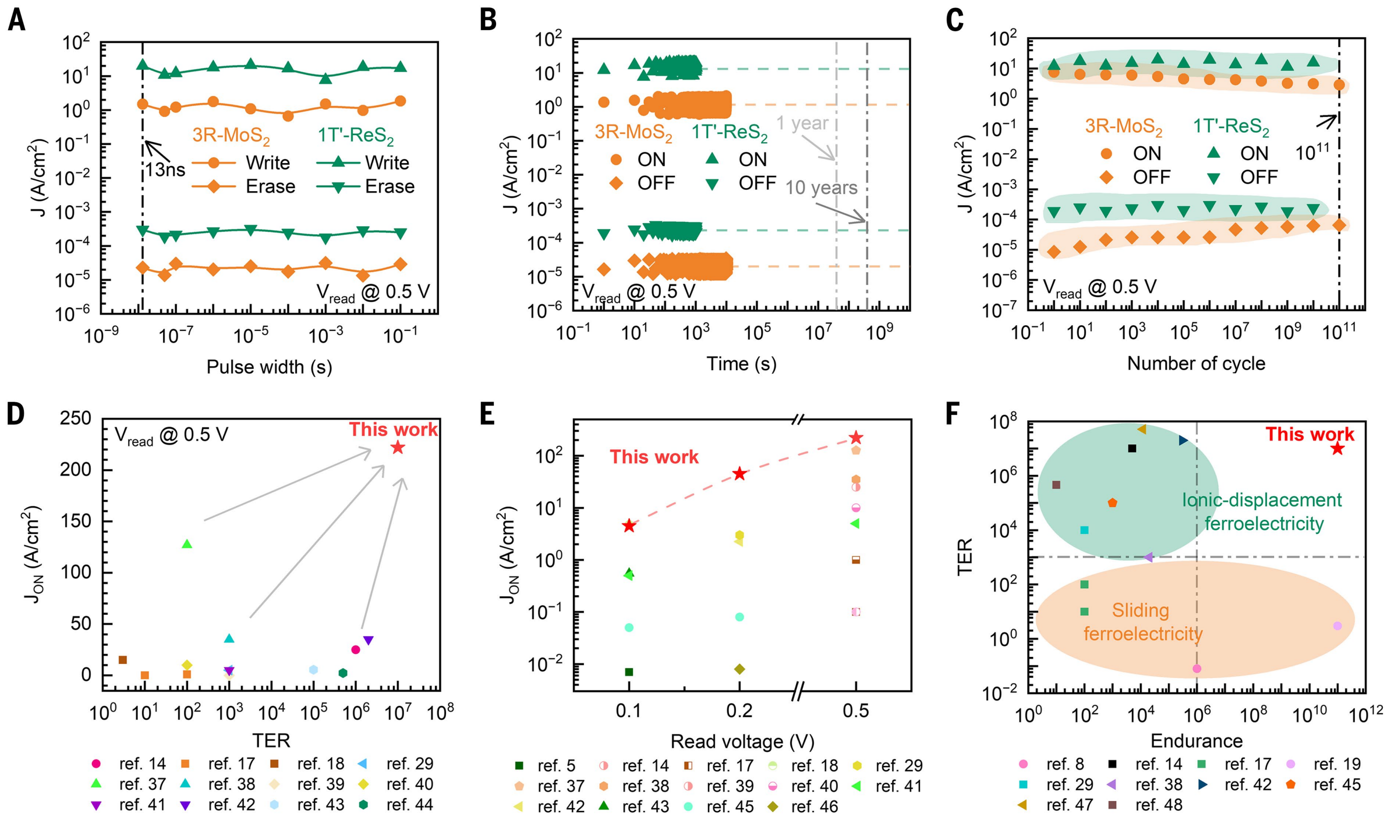

Fig. 4. Performance of the $3R\text{-}MoS_2$ and $1T'\text{-}ReS_2$ sliding FTJs. (**A**) Pulse width–dependent current response of the sliding FTJs. Device current was measured as a function of pulse width under voltage pulse stimulation. The write voltage is +7 V and the erase voltage is −5 V. (**B**) Retention characteristics of the sliding FTJs at room temperature. Measurements showed that the high TER in both devices remained stable over 10^3 to 10^4 seconds and could be projected to 10 years. (**C**) Endurance of the sliding FTJs at room temperature. Measurements were performed using +7 V/−5 V pulses with a width of 100 ns. (**D** and **E**) Benchmark of ON-state current density for different FTJs. Comparison of J_{ON} at 0.5 V and J_{ON} measured across different read voltages for reported FTJs and the device in this work. (**F**) Benchmark of TER versus endurance for different FTJs. The sliding FTJ in this work exhibits a TER exceeding 10^7 and stable polarization switching over 10^{11} cycles.

(*14*, *17*, *18*, *29*, *37–44*), providing strong signal output as well as fast and reliable readout. Across different read voltages, J_{ON} remained consistently high (table S1) (*5*, *14*, *17*, *18*, *37–46*), reflecting robust current modulation. The large J_{ON} provides a large readout margin at a given read bias, enabling faster sensing (shorter integration time) and improved tolerance to parasitic series resistance and interconnect resistance-capacitance in practical FTJ readout circuits, which is particularly beneficial for high-speed operation. In Fig. 4F, a dual-axis plot of TER versus endurance highlights the improvement achieved in this work over previously reported ferroelectric tunneling devices (table S2) (*8*, *14*, *17*, *19*, *29*, *38*, *42*, *45*, *47*, *48*). Our sliding FTJ achieved a high TER $>10^7$ and stable polarization switching up to 10^{11} cycles. In terms of endurance, it outperformed conventional ionic-displacement ferroelectric FTJs (Fig. 4F, green shaded region), which typically exhibit endurance $<10^7$ cycles. Regarding the TER, this device also surpassed other sliding ferroelectric devices (Fig. 4F, orange shaded region), the nonvolatile switching ratios of which are generally <100 (*8*, *19*). These device characteristics make the sliding FTJs promising candidates for data storage and neuromorphic computing (see fig. S11 and SI for the demonstration).

Conclusions

We have demonstrated a high-performance, two-terminal vdW sliding FTJ that overcomes the conventional trade-off between switching endurance and readout contrast. The integration of asymmetric electrodes with an h-BN tunneling barrier amplifies the subtle polarization-induced potential shifts of 2D sliding ferroelectrics into a giant tunneling-current modulation, providing a generalizable design principle for sliding FTJ devices. Our experimental results revealed that the Cr/h-BN/3R-MoS_2/graphene architecture achieved a TER exceeding 10^7 and a robust J_{ON} of 222 A cm^{-2} at a read bias of 0.5 V. These metrics represent a five-order-of-magnitude improvement over previously reported sliding FTJs. Furthermore, the devices exhibit impressive fatigue-resistant operation with an endurance of $>10^{11}$ cycles, combined with a high switching speed of 13 ns and ultralow energy consumption (~6.5 fJ). The generalizability of this design principle is further validated by its successful implementation in the 1T′-ReS_2 system. Given its potential compatibility with back-end-of-line integration, this vdW heterostructure–based platform paves a promising path toward high-density, ultrareliable, and energy-efficient nonvolatile memory and in-memory computing systems.

REFERENCES AND NOTES

1. Z. Wang *et al.*, *Nat. Rev. Mater.* **5**, 173–195 (2020).
2. M. Si, H.-Y. Cheng, T. Ando, G. Hu, P. D. Ye, *MRS Bull.* **46**, 946–958 (2021).
3. M. Hellenbrand, I. Teck, J. L. MacManus-Driscoll, *MRS Commun.* **14**, 1099–1112 (2024).
4. T. Mikolajick, U. Schroeder, S. Slesazeck, *IEEE Trans. Electron Dev.* **67**, 1434–1443 (2020).
5. C. Ma *et al.*, *Nat. Commun.* **11**, 1439 (2020).
6. M. Lanza *et al.*, *Nature* **640**, 613–622 (2025).
7. N. Zheng *et al.*, *Sci. Adv.* **11**, eads0724 (2025).
8. R. Bian *et al.*, *Science* **385**, 57–62 (2024).
9. C. W. Hsu *et al.*, "Self-rectifying bipolar TaOx/TiO_2 RRAM with superior endurance over 1012 cycles for 3D high-density storage-class memory," in *2013 Symposium on VLSI Technology* (IEEE, 2013), pp. T166–T167; https://xplorestaging.ieee.org/document/6576643.
10. J. Zheng *et al.*, *Nat. Commun.* **16**, 5788 (2025).
11. S. Ikeda *et al.*, *Appl. Phys. Lett.* **93**, 082508 (2008).
12. V. Garcia, M. Bibes, *Nat. Commun.* **5**, 4289 (2014).
13. S. H. Park, H. J. Lee, M. H. Park, J. Kim, H. W. Jang, *J. Phys. D Appl. Phys.* **57**, 253002 (2024).
14. J. Wu *et al.*, *Nat. Electron.* **3**, 466–472 (2020).
15. D. Chen, X. Tan, Y. Zhang, J. Jiang, *ACS Appl. Mater. Interfaces* **17**, 22974–22983 (2025).
16. J. Liang *et al.*, *Nat. Nanotechnol.* **20**, 500–506 (2025).
17. J. Kuai *et al.*, *Mater. Res. Express* **8**, 056301 (2021).
18. Y. Wan *et al.*, *Phys. Rev. Lett.* **128**, 067601 (2022).
19. K. Yasuda *et al.*, *Science* **385**, 53–56 (2024).
20. J. Yang *et al.*, *Mater. Horiz.* **9**, 1422–1430 (2022).
21. L. Wang *et al.*, *Nature* **629**, 74–79 (2024).
22. M. Dawber, K. Rabe, J. Scott, *Rev. Mod. Phys.* **77**, 1083–1130 (2005).
23. T. Boscke, J. Muller, D. Braeuhaus, U. Schroder, U. Bottger, *Appl. Phys. Lett.* **99**, 102903 (2011).
24. S. Jiang, Y. Wang, G. Zheng, *Nanomaterials* **15**, 109 (2025).
25. M.-L. Lin, P.-H. Tan, in *Raman Spectroscopy of Two-Dimensional Materials*, P.-H. Tan, Ed. (Springer, 2018), pp. 203–230; https://link.springer.com/chapter/10.1007/978-981-13-1828-3_10.
26. J. van Baren *et al.*, *2D Materials* **6**, 025022 (2019).
27. M. Zhao *et al.*, *Light Sci. Appl.* **5**, e16131–e16131 (2016).
28. S. V. Kalinin, D. A. Bonnell, *Phys. Rev. B Condens. Matter* **65**, 125408 (2002).
29. Y. Wang *et al.*, *Adv. Mater.* **36**, e2410696 (2024).
30. R. Rao *et al.*, *Phys. Rev. B* **99**, 195401 (2019).
31. U. Sharma *et al.*, *Front. Mater.* **10**, 1148979 (2023).
32. H. J. Zhao, L. Bellaiche, X. M. Chen, J. Íñiguez, *Phys. Rev. B* **97**, 054107 (2018).
33. B. B. Tian *et al.*, *Sci. Rep.* **5**, 18297 (2015).
34. J.-N. Heidkamp *et al.*, *Phys. Status Solidi Rapid Res. Lett.* **20**, e202500417 (2026).
35. P. Meng *et al.*, *Nat. Commun.* **13**, 7696 (2022).
36. J.-B. Wu, M.-L. Lin, X. Cong, H.-N. Liu, P.-H. Tan, *Chem. Soc. Rev.* **47**, 1822–1873 (2018).
37. A. Chanthbouala *et al.*, *Nat. Nanotechnol.* **7**, 101–104 (2011).
38. Z. Wen, C. Li, D. Wu, A. Li, N. Ming, *Nat. Mater.* **12**, 617–621 (2013).
39. W. Tang *et al.*, *Small Methods* **6**, e2101583 (2022).
40. D. Zheng *et al.*, *J. Appl. Phys.* **132**, 054101 (2022).
41. X. Du *et al.*, *ACS Appl. Mater. Interfaces* **14**, 1355–1361 (2022).
42. Z. Gao *et al.*, *Device* **1**, 100004 (2023).
43. Q. H. Qin *et al.*, *Adv. Mater.* **28**, 6852–6859 (2016).
44. Z. Luo *et al.*, *Nat. Commun.* **13**, 699 (2022).
45. K. Lee, J. H. Lee, S. H. Baek, J. H. Park, Y. S. Kim, *Appl. Mater. Today* **26**, 101308 (2022).
46. S. Boyn *et al.*, *Appl. Phys. Lett.* **104**, 052909 (2014).
47. J. Li *et al.*, *iScience* **16**, 368–377 (2019).
48. Y. Li *et al.*, *Nano Lett.* **25**, 1680–1688 (2025).
49. Y. Wang, Data for: Giant tunneling electroresistance in sliding ferroelectrics, Zenodo (2026); https://doi.org/10.5281/zenodo.20725435.

ACKNOWLEDGMENTS

Funding: This work was supported by the National Key Research and Development Program of China (grants 2024YFA1409700 and 2023YFA1407000), the National Natural Science Foundation of China (grants 62561160153, 62374158, and U24A20285), the National Natural Science Foundation of China (NSFC)/Research Grants Council (RGC) Joint Research Scheme (grant N_HKU775/25), the RGC General Research Fund (grant 17311325), the Beijing Natural Science Foundation (grant F251001), the Strategic Priority Research Program of the Chinese Academy of Sciences (grant XDB0460000), and the Suzhou Laboratory (grant SZLAB-1208-2025-TS021). **Author contributions:** J.W. conceptualized the project. J.W. and Y.W. performed the investigation. J.W., P.-H.T., H.W., Y.L., Z.W., B.-B.Z., and F.L. provided resources. J.W., Y.W., Y.Zhao, Y.Zhang, C.H., L.Z., Z.Z., and S.L. performed formal analysis. J.W., P.-H.T., H.W., and Z.W. acquired the funding. J.W., P.-H.T., and H.W. supervised and administered the project. Y.W. wrote the original draft. J.W., P.-H.T., H.W., Y.L., Z.W., B.-B.Z., F.L., and Y.W. reviewed and edited the manuscript. All authors discussed the results. **Competing interests:** A provisional Chinese patent has been filed on device architecture of FTJs based on two-dimensional sliding ferroelectrics (application no. 2026108940766 by J.W., Y.W., and P.-H.T., Institute of Semiconductors, Chinese Academy of Sciences). The remaining authors declare no competing interests. **Data, code, and materials availability:** The data for this study are available at Zenodo (*49*).

SUPPLEMENTARY MATERIALS

science.org/doi/10.1126/science.aeh3697
Materials and Methods; Supplementary Text; Figs. S1 to S11; Tables S1 and S2; References (*50–62*)

Submitted 22 March 2026; accepted 20 July 2026

10.1126/science.aeh3697

Giant tunneling electroresistance in sliding ferroelectrics

Yue Wang, Yu Zhao, Yifei Zhang, Liutianyi Zhang, Zijian Zhong, Sishuo Liu, Chentao Hou, Fanxin Liu, Bin-Bin Zhang, Zhongming Wei, Yue-Yang Liu, Han Wang, Ping-Heng Tan, and Jiangbin Wu

Science **393** (6816), . DOI: 10.1126/science.aeh3697

Editor's summary

A two-terminal ferroelectric tunnel junction based on two-dimensional sliding ferroelectrics achieved the high switching endurance and readout contrast needed for low-power memory devices. Fatigue-resistant sliding ferroelectrics such as 3R-MoS_2 often have weak readout in two-terminal devices because of their small remanent polarization. Wu *et al*. engineered a 3R-MoS_2 ferroelectric tunnel junction with an h-BN tunneling barrier and a weakly screening monolayer graphene electrode that amplified polarization transduction by modulating the tunneling barrier profile and carrier injection and extraction. The devices had a tunneling electroresistance of greater than 10^7, an endurance of more than 10^{11} cycles, and an estimated switching energy of 6.5 femtojoules. —Phil Szuromi

Science (ISSN 1095-9203) is published by the American Association for the Advancement of Science. 1200 New York Avenue NW, Washington, DC 20005. The title *Science* is a registered trademark of AAAS.